RESEARCH ARTICLE

CHEMISTRY

Plastics-to-syngas photocatalysed by Co–Ga$_2$O$_3$ nanosheets

Jiaqi Xu [iD][1,3,†], Xingchen Jiao[1,†], Kai Zheng[1,†], Weiwei Shao[1], Shan Zhu[1], Xiaodong Li[1], Junfa Zhu[1], Yang Pan[1], Yongfu Sun[1,2,*] and Yi Xie[1,2]

ABSTRACT

Plastics take hundreds of years to degrade naturally, while their chemical degradation typically requires high temperature and pressure. Here, we first utilize solar energy to realize the sustainable and efficient plastic-to-syngas conversion with the aid of water at ambient conditions. As an example, the commercial plastic bags could be efficiently photoconverted into renewable syngas by Co–Ga$_2$O$_3$ nanosheets, with hydrogen and carbon monoxide formation rates of 647.8 and 158.3 μmol g^{-1} h^{-1}. *In situ* characterizations and labelling experiments unveil water is photoreduced into hydrogen, while non-recyclable plastics including polyethylene bags, polypropylene boxes and polyethylene terephthalate bottles are photodegraded into carbon dioxide, which is further selectively photoreduced into carbon monoxide. In-depth investigation illustrates that the efficiency of syngas production mainly depends on the carbon dioxide reduction process and hence photocatalysts of high carbon dioxide reduction activity should be designed to promote the efficiency of plastic-to-syngas conversion in the future. The concept for the photoreforming of non-recyclable plastics into renewable syngas helps to eradicate 'white pollution' and alleviate the energy crisis simultaneously.

Keywords: commercial plastics, syngas, photoconversion, CO$_2$ reduction, ambient conditions

[1]Hefei National Laboratory for Physical Sciences at Microscale, National Synchrotron Radiation Laboratory, University of Science and Technology of China, Hefei 230026, China; [2]Institute of Energy, Hefei Comprehensive National Science Center, Hefei 230031, China and [3]Key Laboratory of Green Chemistry & Technology, Ministry of Education, College of Chemistry, Sichuan University, Chengdu 610064, China

*Corresponding author. E-mail: yfsun@ustc.edu.cn
†Equally contributed to this work.

INTRODUCTION

Plastic products, such as shopping bags, meal boxes and mineral-water bottles, have become one of the most widely used man-made materials in our daily life. It is estimated that ∼359 million tons of plastics are produced annually in the world and a total of ∼12 000 million metric tons of non-recyclable plastic wastes will have accumulated in the natural environment by 2050 [1]. Although these non-recyclable plastic wastes could spontaneously degrade over hundreds of years, they may also turn into microplastics that will invade water, plants and animals, and eventually transfer into the human body [2,3]. Recently, the World Health Organization announced that >90% of the prevailing bottled water that was tested contained more or less microplastics. Also, Mason *et al.* have reported that the microplastic concentrations of some bottled water could amount to >10 000 particles per liter [4]. More surprisingly, Schwabl *et al.* have confirmed that microplastics

had for the first time been detected in human stools, implying unintentional ingestion of microplastics by humans [5]. All these studies suggest that non-recyclable plastic wastes in the environment are encroaching on human health. However, owing to their high stability and durability, it is still very difficult to rapidly degrade or sustainably recycle these discarded plastics [6,7]. Aside from the most widely used method of landfill, traditional strategies including pyrolysis and hydrocracking for the degradation of these non-recyclable plastic wastes usually require a high temperature up to 500°C [8]. Considering the abundant carbon sources of plastic wastes, they may serve as the raw material for the production of high-value-added fuels, for which many novel techniques have been employed to convert these non-recyclable plastic wastes into useful carbon-based compounds [9]. For example, Reisner *et al.* have realized the photoreforming of polyethylene terephthalate (PET) and polylactic

acid (PLA) into hydrogen (H_2) and some valuable carbon-based chemicals with the help of $CN_x|Ni_2P$ catalysts and alkaline aqueous conditions [10], while they have also converted polyethylene (PE) into hydrocarbons through the integrated tandem chemical-photo/electrocatalytic processes [11]. Inspired by these great breakthroughs, it is a promising technology for utilizing solar energy to convert the non-recyclable plastic wastes into useful carbon-based compounds through a green and economic pathway.

In this regard, renewable syngas, primarily comprising carbon monoxide (CO) and H_2, may be a promising target product since it could act as a versatile ingredient for preparing hydrocarbon fuels (methanol, ethanol, etc.) as well as hydrocarbon building blocks like ethylene and propylene [12]. To date, syngas is mainly produced by the reformation of fossil fuels, including coal, oil and natural gas, under rigorous and costly conditions (e.g. high temperature and pressure) [13,14]. For example, Ma *et al.* reported that the FeCralloy woven fiber-based catalyst could convert natural gas into CO and H_2 at a temperature of 900°C and pressure of 0.1–2 MPa [15], while Zhou *et al.* demonstrated that the gasification of coal could produce CO, H_2, methane (CH_4) and carbon dioxide (CO_2) at 700°C and 3.5 MPa [16]. Obviously, these strategies not only demand high energy consumption, but also result in a variety of complex by-products. In this case, the utilization of plastic wastes as feedstock for clean and renewable syngas production can contribute to the eradication of plastic pollution and the alleviation of a potential energy crisis simultaneously. Bearing in mind the discussion above, it is urgent to develop novel strategies for sustainably and efficiently converting non-recyclable plastic wastes into renewable syngas under mild conditions.

Herein, we first propose a sustainable and eco-friendly strategy for the photoreforming of non-recyclable plastics into clean renewable syngas with the assistance of H_2O at ambient temperature and pressure. In this process, H_2O could be photoreduced into H_2, while various commercial plastics including PE bags, polypropylene (PP) boxes and PET bottles could be photodegraded into CO (Scheme S1). Compared with the time-consuming spontaneous degradation of plastics, the utilization of sunlight and suitable photocatalysts can help to realize the fast and sustainable conversion of plastics into renewable syngas, which could be further recycled to the plastics through the Fischer-Tropsch synthesis and polymerization processes.

RESULTS AND DISCUSSION

Based on the aforementioned analysis, reasonable selection of highly active photocatalysts holds the key for realizing plastic degradation, CO_2 reduction and H_2O splitting to produce renewable syngas. Given this, earth-abundant and environmentally friendly Ga_2O_3 could be selected as a representative example to investigate the plastic-to-syngas conversion performance [17], since its valence-band (VB) maximum at approximately +3.16 V vs. NHE and conduction-band (CB) minimum at approximately −1.62 V vs. NHE at pH = 0 could satisfy some key redox potentials of CO_2/CO (−0.1 V), H^+/H_2 (0 V) or O_2/H_2O (1.23 V), and even $\cdot OH/H_2O$ (2.73 V) that may take place in the photoconversion process [18,19]. However, the wide band gap of Ga_2O_3 may inversely result in lower photocatalytic performance owing to the poor solar energy utilization efficiency. In this regard, heteroatom doping can be utilized to tailor the electronic structure of Ga_2O_3, which could not only extend their photoabsorption, but also accelerate the carrier separation efficiency [20]. More importantly, it could provide a plentiful surface of exposed atoms by downsizing the materials into atomic thickness, which could act as highly active catalytic sites to boost the photoconversion property [21]. Accordingly, we employ Co-doped Ga_2O_3 (Co–Ga_2O_3) nanosheets and pristine Ga_2O_3 nanosheets as ideal models to explore the plastic-into-syngas process under mild conditions.

To this end, Co–Ga_2O_3 nanosheets were successfully fabricated for the first time. As displayed in Fig. S1, their XRD pattern could be indexed to γ-Ga_2O_3 (JCPDS card No. 19-4506). The transmission electron microscopy (TEM) image in Fig. S2 clearly reveals their ultra-thin morphology, while the high-resolution TEM image in Fig. S3A shows that the lattice plane spacings of Co–Ga_2O_3 nanosheets were 0.25 and 0.24 nm with a dihedral angle of 30°, in accordance with the calculated angle between the (113) and (222) planes of γ-Ga_2O_3, suggesting their [1 –1 0] orientation. The atomic force microscopy image in Fig. S3B and C indicates their average thickness of ∼1.05 nm, consisting well with the thickness of 12 atoms along the [1 –1 0] direction of γ-Ga_2O_3. More importantly, the annular dark-field TEM image and element mapping in Fig. S4 depict the homogeneous distribution of Ga, O and Co elements, while their X-ray photoelectron spectra of the Co 2p core level in Fig. S5 exhibits two feature satellite peaks at 787.1 and 804.1 eV, verifying the introduction of Co^{2+} in the synthetic sample [22]. For comparison, pristine Ga_2O_3 nanosheets with the same orientation and thickness were also

fabricated by virtue of a similar synthetic strategy (Figs S1, S6 and S7). Furthermore, UV–vis diffuse reflectance spectra and synchrotron-radiation photoemission spectroscopy were utilized to unravel the electronic band structures for the Co–Ga_2O_3 nanosheets and the Ga_2O_3 nanosheets (Figs S8 and S9). Based on these results, it was demonstrated that the VB edge and the CB edge for the Co–Ga_2O_3 nanosheets were located at 2.50 and –1.40 V vs. NHE at pH = 7, while the VB and CB edges for the Ga_2O_3 nanosheets were located at 3.19 and –1.46 V vs. NHE at pH = 7. Thus, one can conclude that both of them are capable of realizing some key reactions such as H_2O oxidation or CO_2, O_2 and H_2O reduction [23,24].

To disclose whether these two photocatalysts can realize the sustainable conversion of non-recyclable plastics into clean renewable syngas under mild conditions, the commonly used commercial plastic products of PE plastic bags, PP plastic boxes and PET plastic bottles were taken as the examples to perform the photocatalytic experiments, wherein the synthetic samples and the commercial plastics were mixed in pure water and irradiated by simulated sunlight (AM 1.5 G, 100 mW/cm^2) at ambient temperature and pressure. Commercial plastic products of PE plastic bags, PP plastic boxes and PET plastic bottles were initially shredded into powders with a size of <5 mm using a pulverizer (Figs S10–S12). It should be mentioned that small plastics (≤5 mm) were commonly defined as the microplastics, which were particularly difficult to be recycled and may cause some unpredictable damage to the ecosystem. As displayed in Fig. 1a–c, Figs S13–S17 and Tables S1 and S2, the powders of commercial PE plastic bags, PP plastic boxes and PET plastic bottles could be efficiently photodegraded by both the Co–Ga_2O_3 nanosheets and the Ga_2O_3 nanosheets, in which the gas products of H_2, CO and CO_2 were detected by gas chromatography, while there was no detectable liquid product confirmed by the ^{1}H NMR spectra in Fig. S13. Interestingly, there was plenty of CO_2 dissolved in the water (Tables S5 and S6). It is worth noting that a handful of microplastics with smaller size were also detected (Fig. S14), which might have been produced during the photoconversion processes, conforming to the principle of carbon balance (please see the Methods section). Taking the commercial PE plastic bags as an example, the evolution rates of H_2, CO and CO_2 for the Co–Ga_2O_3 nanosheets were 647.8, 158.3 and 419.3 μmol g^{-1} h^{-1}—roughly 1.6, 1.9 and 1.6 times higher than those of the Ga_2O_3 nanosheets, implying the former's better photoconversion performance. Note that the weight loss for the commercial PE plastic bags was 53% after 24 h irradiation over

the Co–Ga_2O_3 nanosheets and the weight loss could reach 81% after 48 h irradiation (Fig. S15). More importantly, upon adding another 100 mg of commercial PE plastic bags to the photocatalytic system after 24 h irradiation, the Co–Ga_2O_3 nanosheets also possessed almost the same formation rates of H_2, CO and CO_2 (Fig. S16), suggesting their superb photocatalytic stability. Consequently, the commercial plastic products including PE plastic bags, PP plastic boxes and PET plastic bottles could be efficiently photodegraded into CO, while H_2O could be photoreduced into H_2 by the Co–Ga_2O_3 nanosheets.

To unveil the origin of the generated products, the photoreforming of reagent-grade PE was carried out over the Co–Ga_2O_3 nanosheets in an air atmosphere at ambient temperature and pressure with simulated sunlight. The evolution rates of H_2, CO and CO_2 were 692.0, 177.8 and 476.4 μmol g^{-1} h^{-1} (Fig. S17)—slightly higher than those for the commercial PE plastic bags. Of note, control experiments showed that H_2 was detected, while there was no detectable CO and CO_2 without reagent-grade PE in the photocatalytic system, suggesting that H_2 may have come from the reduction of H_2O (Table S3). To further disclose the origin of the H_2, the photoreforming experiment of reagent-grade PE over the Co–Ga_2O_3 nanosheets was performed in the pure D_2O solvent. Note that the synchrotron-radiation vacuum UV photoionization mass spectrometry (SVUV-PIMS) in Fig. 2a demonstrates that only D_2 was detected in the D_2O solvent, which firmly affirmed that the generated H_2 originated from the H_2O rather than the PE during the photoreforming processes. Moreover, when the light or photocatalyst or reagent-grade PE was removed, there was no detectable CO and CO_2 (Table S3), verifying that CO and CO_2 originated from the photodegradation of PE by the photocatalyst. Furthermore, H_2 and O_2 could be detected when no PE powders were added into the photocatalytic system under a N_2 atmosphere (Fig. S18), implying that the H_2O splitting could have been triggered by these two photocatalysts, in which some amount of H_2O_2 was also produced during the process (Fig. S19). To further testify the origin of the CO_2 and CO, AgNO$_3$ was added into the solution, which helped to clearly identify the photo-oxidation products since AgNO$_3$ was usually considered as a trapping agent to efficiently consume the photo-generated electrons [25]; during the corresponding photocatalytic process, only CO_2 was detected (Fig. 2d and Table S4), which certified that CO_2 indeed derived from the photo-oxidation of PE. This result also indicated that CO may be generated from CO_2 photoreduction, further attested to by the corresponding $^{13}CO_2$ isotope-labelling experiments in Fig. S20.
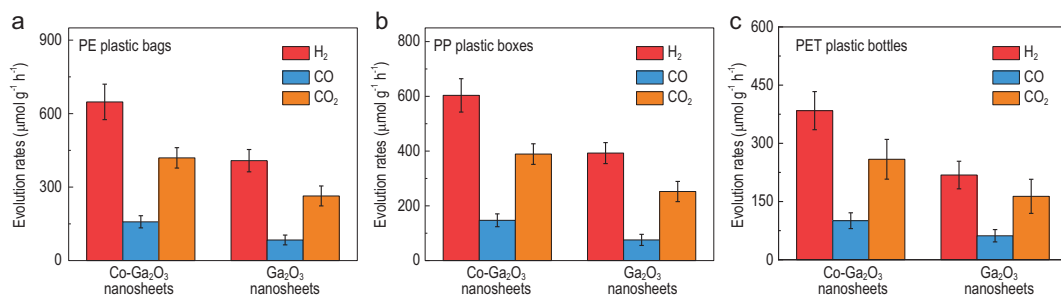
Figure 1. Efficient photoconversion of various plastics into syngas over Co–Ga_2O_3 nanosheets under mild conditions. Photoconversion of (a) commercial PE plastic bags, (b) commercial PP plastic boxes and (c) commercial PET plastic bottles under simulated AM 1.5G solar irradiation at ambient temperature and pressure: the formation rates of H_2 (red), CO (blue) and CO_2 (yellow) for Co–Ga_2O_3 nanosheets and Ga_2O_3 nanosheets in 24 h. The error bars in (a)–(c) represent the standard deviations of three independent measurements.
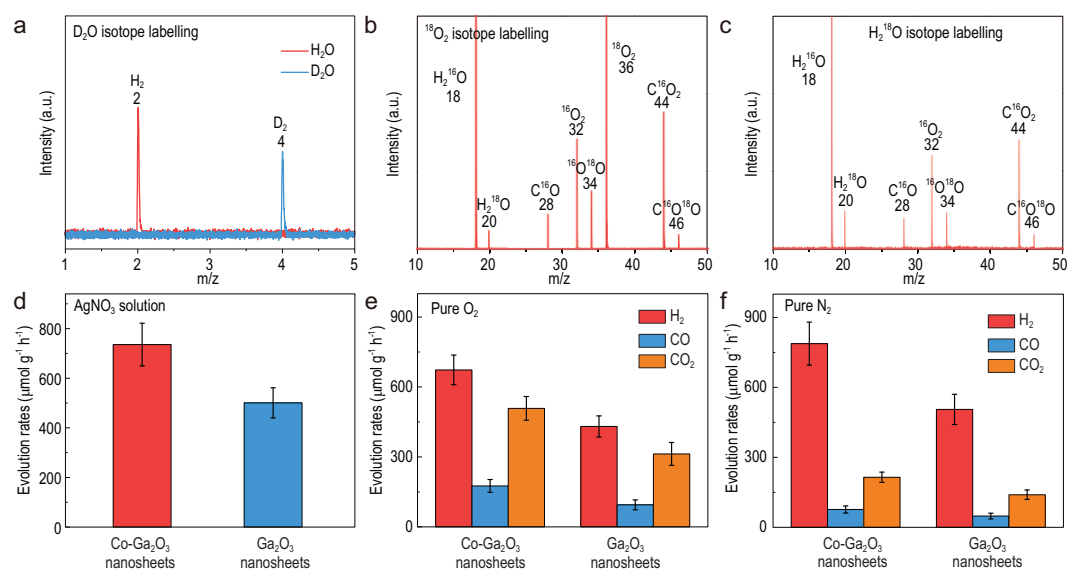
Figure 2. Investigation of mechanism involved in the photoconversion of reagent-grade PE into syngas over Co–Ga_2O_3 nanosheets. Synchrotron-radiation vacuum UV photoionization mass spectrometry (SVUV-PIMS) for the gas products in (a) the H_2O and D_2O isotope-labelling experiments after 24 h irradiation at $h\nu = 16.5\,eV$; (b) $^{18}O_2$ and (c) $H_2^{18}O$ isotope-labelling experiments after 24 h irradiation at $h\nu = 14.5\,eV$. (d) The formation rates of CO_2 (no H_2 or CO was detected) in 2 mmol/L $AgNO_3$ solution, (e) the products in the pure O_2 atmosphere, (f) the products in the pure N_2 atmosphere. The error bars in (d)–(f) represent the standard deviations of three independent measurements.

During the experiment of $^{13}CO_2$ photoreduction in pure water, only ^{13}CO was detected, which clearly affirmed that the generated CO stemmed from the reduction of CO_2. Furthermore, when the reaction atmosphere changed from air to high-purity O_2, the yields of CO and CO_2 did not exhibit noticeable differences (Fig. 2e and Table S4). However, the yields of CO and CO_2 for the Co–Ga_2O_3 nanosheets obviously decreased to 76.5 and 214.7 μmol g^{-1} h^{-1} in the high-purity N_2 atmosphere (Fig. 2f and Table S4), hinting that O_2 should be beneficial to the photoreforming processes. Additionally, the $^{18}O_2$ isotope-labelling experiments in Fig. 2b clearly show the presence of $C^{16}O^{18}O$, demonstrating that O_2 was indeed involved in the PE degradation

processes. The identification of $C^{16}O^{18}O$ in the $H_2^{18}O$ labelling experiments (Fig. 2c) also implied the participation of H_2O in the photodegradation of PE. Moreover, upon removing $H_2^{18}O$ and $^{18}O_2$ from the reaction system, there was no detectable $C^{16}O^{18}O$ (Fig. S21), further confirming that H_2O and O_2 participated in the oxidation of PE into CO_2. From the above-mentioned results, we deduce that the H_2 stemmed from the H_2O instead of the PE, while both the O_2 and H_2O took part in the oxidation of PE into CO_2 and then the formed CO_2 could be further reduced to CO.

To further understand the PE photoreforming processes, *in situ* electron spin resonance (ESR) spectra were employed to identify the reaction
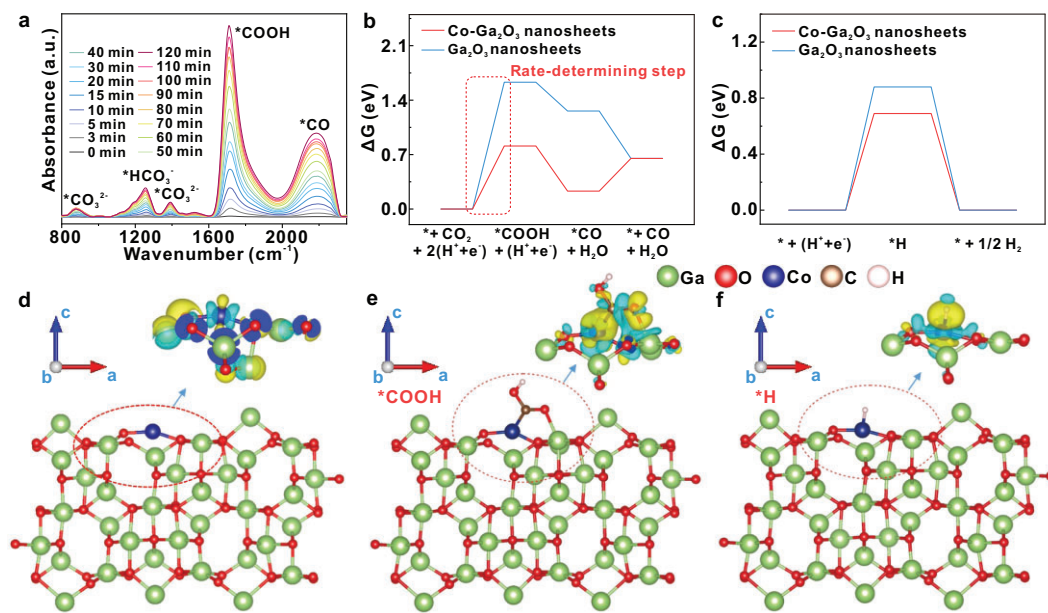
Figure 3. Investigation of Co atoms in the Co–Ga$_2$O$_3$ nanosheets for the plastic-to-syngas process. (a) *In situ* FT-IR spectra of Co–Ga$_2$O$_3$ nanosheets for the CO$_2$ photoreduction process. Free-energy diagrams of (b) CO$_2$ photoreduction to CO and (c) H$_2$O photoreduction to H$_2$ for the Co–Ga$_2$O$_3$ nanosheets and the Ga$_2$O$_3$ nanosheets. (d) The differential charge density map of the Co–Ga$_2$O$_3$ nanosheets. The differential charge density maps of (e) *COOH and (f) H* on the Co–Ga$_2$O$_3$ nanosheets. The yellow and blue contours in (d)–(f) manifest electron accumulation and depletion, and the values of isosurfaces in (d)–(f) are 0.007 and 0.002 eÅ^{-3}, respectively.

intermediates, where 5,5-dimethyl-1-pyrroline N-oxide (DMPO) was used as the spin-trapping agent. The ESR signals in Fig. S22 exhibit a 1 : 2 : 2 : 1 quartet pattern in the water solution, which could be assigned to the ·OH captured by the DMPO [26]. Combined with the H$_2^{18}$O isotope-labelling experiments in Fig. 2c, it is reasonable to deduce that H$_2$O would be oxidized into ·OH radicals by the photoinduced holes and then the ·OH radicals would participate in the oxidation processes of the PE. Meanwhile, the ESR signals in Fig. S23 show a quartet pattern with an intensity of nearly 1 : 1 : 1 : 1 in the methanol solution, which could be assigned to the superoxide radicals (O$_2^{\bullet-}$) captured by the DMPO [27]. As revealed in Fig. S24, the UV−vis absorption spectra for the reaction solution after 24 h irradiation displayed a characteristic peak at 436 nm, which could be ascribed to the characteristic peak of H$_2$O$_2$ [28]. Considering that O$_2$ is in favor of the photodegradation of PE powders, it is possible that the O$_2$ may undergo stepwise photoreduction into O$_2^{\bullet-}$, H$_2$O$_2$ and H$_2$O. Besides, the detection of C^{16}O^{18}O in both the H$_2^{18}$O and ^{18}O$_2$ labelling experiments suggested that both the ·OH radicals and the O$_2$ participate in the photo-oxidation of PE into CO$_2$. To gain in-depth investigation of the CO formation process, photocatalytic experiments in pure CO$_2$ were conducted over the Co–Ga$_2$O$_3$ nanosheets, in which *in situ* FTIR spectra were per-

formed to trace the reaction intermediates. As revealed in Fig. 3a, the new peak that appeared at ∼1710 and ∼2180 cm^{-1} under irradiation could be assigned to the *COOH and *CO groups, respectively [29,30]. It meant that CO$_2$ molecules were initially reduced into COOH* intermediates by the incoming proton–electron pair (H$^+$ + e$^-$); then, the COOH* intermediates might have coupled with another H$^+$ + e$^-$ pair to form the *CO intermediates, which would be liberated from the surface of the catalyst to form free CO molecules [31].
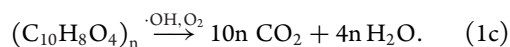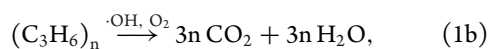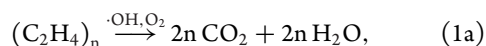
From what has been mentioned above, it was concluded that the mechanism of photoconverting commercial plastics and H$_2$O into syngas could be proposed as the following procedure. Under light irradiation, the photocatalysts initially generated electrons and holes pairs, which could react with the H$_2$O to form H$_2$ and O$_2$. Then, the ·OH radicals derived from H$_2$O and the produced O$_2$ or O$_2$ in the air atmosphere could synchronously photodegrade plastics into CO$_2$; and meanwhile, O$_2$ was also reduced to O$_2^{\bullet-}$, H$_2$O$_2$ and H$_2$O in order by the photoexcited electrons. Subsequently, the generated CO$_2$ would be further reduced into CO through *COOH intermediates, while H$_2$O was oxidized into O$_2$. In short, photoconverting commercial plastics and H$_2$O into syngas may undergo the following three steps in sequence (Scheme 1):
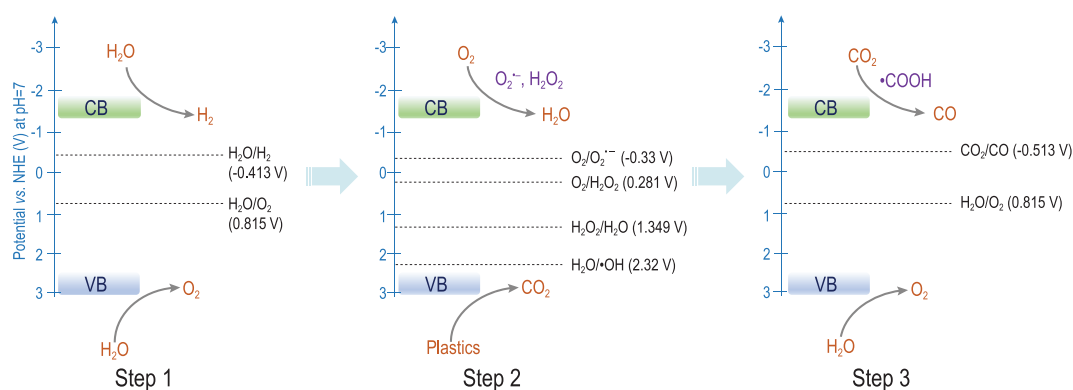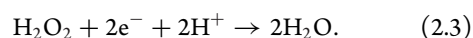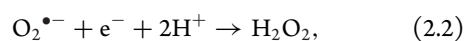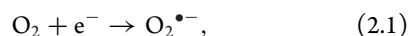
Scheme 1. Schematic representation of the proposed mechanism for the photoconversion of non-recyclable plastics into renewable syngas under mild conditions.
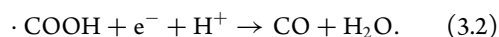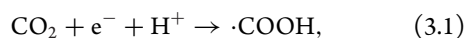
Step 1: H_2O was initially split into H_2 and O_2.
Step 2: Plastics were oxidized into CO_2:

$$(C_2H_4)_n \xrightarrow{\cdot OH, O_2} 2n\,CO_2 + 2n\,H_2O, \qquad (1a)$$

$$(C_3H_6)_n \xrightarrow{\cdot OH, O_2} 3n\,CO_2 + 3n\,H_2O, \qquad (1b)$$

$$(C_{10}H_8O_4)_n \xrightarrow{\cdot OH, O_2} 10n\,CO_2 + 4n\,H_2O. \qquad (1c)$$

Synchronously, O_2 was reduced to H_2O:

$$O_2 + e^- \rightarrow O_2^{\bullet -}, \qquad (2.1)$$

$$O_2^{\bullet -} + e^- + 2H^+ \rightarrow H_2O_2, \qquad (2.2)$$

$$H_2O_2 + 2e^- + 2H^+ \rightarrow 2H_2O. \qquad (2.3)$$

Step 3: CO_2 was further reduced to CO:

$$CO_2 + e^- + H^+ \rightarrow \cdot COOH, \qquad (3.1)$$

$$\cdot COOH + e^- + H^+ \rightarrow CO + H_2O. \qquad (3.2)$$

Meanwhile, H_2O was oxidized to O_2.

After disclosing the PE photoreforming processes, it is necessary to uncover the reasons for the boosted plastics photoconversion performance of Co–Ga_2O_3 nanosheets. Owing to the d–d internal transitions, the Co–Ga_2O_3 nanosheets possessed obviously enhanced photoabsorption relative to the Ga_2O_3 nanosheets (Fig. S8), which indicated that the former could make better use of the photon energy and generate more charge carriers to engage in the plastics photoreforming processes [18]. In addition, density-functional-theory calculations showed that the Co–Ga_2O_3 nanosheets possessed distinctly enhanced density of states at the VB edge (Fig. S25), which contributed to the promoted photocarrier transfer ability, and hence helped to provide more photo-generated electrons and holes to participate in the subsequent redox reactions [20]. Moreover, the photoluminescence (PL) intensity dramatically decreased after the introduction of Co atoms into the Ga_2O_3 nanosheets, indicating the restrained recombination efficiency of photo-generated electron–hole pairs (Fig. S26) [32]. Importantly, the CO_2 temperature-programmed desorption spectra in Fig. S27 manifested that the onset desorption temperature of CO_2 for the Co–Ga_2O_3 nanosheets (88°C) was higher than that of the Ga_2O_3 nanosheets (76°C), suggesting that the former has stronger adsorption behavior for CO_2, which is beneficial to the further reduction of CO_2 [33]. Furthermore, as uncovered by Fig. 3b and Tables S7 and S8, the calculated reaction Gibbs free energies (ΔG) showed that the rate-determining step of CO_2 photoreduction into CO was the formation of *COOH intermediates, wherein the Co–Ga_2O_3 nanosheets possessed a lower COOH* intermediates formation energy compared with the Ga_2O_3 nanosheets. This could be attributed to the fact that the introduction of Co atoms caused the charge accumulation of the Co atoms and the neighboring Ga atoms, which was conducive to stabilizing the *COOH intermediates through Co–Ga dual active sites and hence lowered its formation energy (Fig. 3d and e, and Figs S28 and S29) [34]. More importantly, the calculated reaction Gibbs free energies in Fig. 3c and Fig. S30 disclose that the rate-determining step of H_2O reduction into H_2 was the formation of H* intermediates, in which the Co–Ga_2O_3 nanosheets possessed a lower H* intermediates formation energy with respect to the Ga_2O_3 nanosheets. This might be ascribed to the charge accumulation of the Co–H bond induced by the introduced Co atoms, which helped to stabilize

the H* intermediates, thus lowering the formation energy (Fig. 3f). As a result, both theoretical and experimental results affirmed that introducing Co atoms into Ga_2O_3 nanosheets as the active sites can simultaneously favor the processes of CO_2 reduction into CO and H_2O reduction into H_2 through stabilizing the *COOH and H* intermediates. That is to say, the presence of Co atoms could make for lowing the activation energies of CO_2 reduction and H_2O splitting, and hence promote the property of plastic-to-syngas photoconversion.

CONCLUSION

In conclusion, we first realized the sustainable and efficient conversion of non-recyclable plastics into renewable syngas in pure water at ambient temperature and pressure. In this process, H_2O is photoreduced into H_2, while non-recyclable plastics including PE plastic bags, PP plastic boxes and PET plastic bottles are photodegraded into CO_2, which is further selectively photoreduced into CO. As an example, commercial PE plastic bags could be efficiently photoconverted into syngas with the aid of H_2O by the Co–Ga_2O_3 nanosheets, in which the H_2 and CO formation rates were ~647.8 and ~158.3 μmol g^{-1} h^{-1} —roughly 1.6 and 1.9 times higher than those of the Ga_2O_3 nanosheets, respectively. More importantly, the weight losses of PE plastic bags, PP plastic boxes and PET plastic bottles were up to approximately 81%, 78% and 72% after 48 h irradiation over the Co–Ga_2O_3 nanosheets. Through deeply exploring the mechanism of plastics photoconversion into syngas, it can be concluded that the whole efficiency is mainly dependent on the process of CO_2 reduction into CO, and hence it is necessary to design photocatalysts of high CO_2 reduction activity to promote the efficiency of non-recyclable plastics degradation in the future. Meanwhile, considering that the residual microplastics in aqueous solution are hard to fully degrade, some precautionary measures such as filtration units and advanced wastewater treatment technologies like membrane filtration may be needed in the future. Briefly, the design concept may help to open up new avenues toward the curbing of white pollution and the relieving of the energy crisis simultaneously.

METHODS
Synthesis of the Co-doped Ga_2O_3 (Co–Ga_2O_3) nanosheets

In a typical synthetic procedure, 256 mg $Ga(NO_3)_3$ and 29 mg $Co(NO_3)_2 \cdot 6H_2O$ were added to 5 mL water with vigorous stirring for 10 min. Then, 30 mL triethylenetetramine (TETA) was added to the solution after continuous magnetic stirring for another 30 min. Finally, the solution was transferred to a stainless Teflon-lined autoclave, which was sealed and maintained at 160°C for 48 h. The product was collected by centrifugation, washed thoroughly with absolute ethanol and deionized water several times, and then dried at 60°C for 12 h.

Synthesis of the Ga_2O_3 nanosheets

The procedures were the same as those for the Co–Ga_2O_3 nanosheets, except no $Co(NO_3)_2 \cdot 6H_2O$ was added.

SUPPLEMENTARY DATA

Supplementary data are available at *NSR* online.

ACKNOWLEDGEMENTS

FUNDING

AUTHOR CONTRIBUTIONS

Y.X., Y.F.S., J.Q.X., X.C.J. and K.Z. conceived of the idea and co-wrote the paper. J.Q.X., X.C.J., W.W.S., S.Z., J.F.Z. and Y.P. carried out the sample synthesis, characterization and carbon dioxide photoreduction measurement. J.Q.X carried out the first-principles calculations. All the authors discussed the results, and commented on and revised the manuscript.

Conflict of interest statement. None declared.

REFERENCES

1. Geyer R, Jambeck JR and Law KL. Production, use, and fate of all plastics ever made. *Sci Adv* 2017; **3**: e1700782.
2. Seltenrich N. New link in the food chain? Marine plastic pollution and seafood safety. *Environ Health Perspect* 2015; **123**: A34.
3. Rochman CM, Hoh E and Kurobe T *et al.* Ingested plastic transfers hazardous chemicals to fish and induces hepatic stress. *Sci Rep* 2013; **3**: 3263.
4. Mason SA, Welch VG and Neratko J. Synthetic polymer contamination in bottled water. *Front Chem* 2018; **6**: 407.
5. Schwabl P, Koppel S and Konigshofer P *et al.* Detection of various microplastics in human stool a prospective case series. *Ann Intern Med* 2019; **171**: 453–7.
6. Tournier V, Topham CM and Gilles A *et al.* An engineered PET depolymerase to break down and recycle plastic bottles. *Nature* 2020; **580**: 216–9.
7. Garcia JM and Robertson ML. The future of plastics recycling chemical advances are increasing the proportion of polymer waste that can be recycled. *Science* 2017; **358**: 870–2.
8. Nisar J, Ali M and Awan IA. Catalytic thermal decomposition of polyethylene by pyrolysis gas chromatography. *J Chil Chem Soc* 2011; **56**: 653–5.
9. Estahbanati MR, Kong XY and Eslami A *et al.* Current developments in the chemical upcycling of waste plastics using alternative energy sources. *ChemSusChem* 2021; **14**: 4152–66.
10. Uekert T, Kasap H and Reisner E *et al.* Photoreforming of nonrecyclable plastic waste over a carbon nitride/nickel phosphide catalyst. *J Am Chem Soc* 2019; **141**: 15201–10.
11. Pichler CM, Bhattacharjee S and Rahaman M *et al.* Conversion of polyethylene waste into gaseous hydrocarbons via integrated tandem chemical-photo/electrocatalytic processes. *ACS Catal* 2021; **11**: 9159–67.
12. Nguyen VN and Blum L. Syngas and synfuels from H_2O and CO_2: current status. *Chem Ing Tech* 2015; **87**: 354–75.
13. Chen LW, Gangadharan P and Lou HH. Sustainability assessment of combined steam and dry reforming versus tri-reforming of methane for syngas production. *Asia-Pac J Chem Eng* 2018; **13**: e2168.
14. Gur M and Canbaz ED. Analysis of syngas production and reaction zones in hydrogen oriented underground coal gasification. *Fuel* 2020; **269**: 117331.
15. Ma ZN, Ouzilleau P and Trevisanut C *et al.* Partial oxidation of methane to syngas over Pt/Rh/MgO catalyst supported on FeCralloy woven fibre. *Can J Chem Eng* 2016; **94**: 642–9.
16. Zhou X, Zhao J and Guo S *et al.* High quality syngas production from pressurized K_2CO_3 catalytic coal gasification with in-situ CO_2 capture. *Int J Hydrogen Energy* 2018; **43**: 17091–9.
17. Sun H, Zhang L and Yu J *et al.* Phase junction enhanced photocatalytic activity of Ga_2O_3 nanorod arrays on flexible glass fiber fabric. *RSC Adv* 2020; **10**: 11499–506.
18. Chang XX, Wang T and Gong JL. CO_2 photo-reduction: insights into CO_2 activation and reaction on surfaces of photocatalysts. *Energy Environ Sci* 2016; **9**: 2177–96.
19. Navarrete M, Cipagauta DS and Gómez R. Ga_2O_3/TiO_2 semiconductors free of noble metals for the photocatalytic hydrogen production in a water/methanol mixture. *J Chem Technol Biotechnol* 2019; **94**: 3457–65.
20. Kikkawa S, Teramura K and Asakura H *et al.* Development of Rh-doped Ga_2O_3 photocatalysts for reduction of CO_2 by H_2O as an electron donor at a more than 300 nm wavelength. *J Phys Chem C* 2018; **122**: 21132–9.
21. Sun Z, Talreja N and Tao H *et al.* Catalysis of carbon dioxide photoreduction on nanosheets: fundamentals and challenges. *Angew Chem Int Ed* 2018; **57**: 7610–27.
22. Xu J, Li X and Ju Z *et al.* Visible-light-driven overall water splitting boosted by tetrahedrally coordinated blende cobalt(II) oxide nanosheets. *Angew Chem Int Ed* 2019; **58**: 3032–6.
23. Wood PM. The potential diagram for oxygen at pH 7. *Biochem J* 1988; **253**: 287–9.
24. Sun Z, Ma T and Tao H *et al.* Fundamentals and challenges of electrochemical CO_2 reduction using two-dimensional materials. *Chem* 2017; **3**: 560–87.
25. Allen MR, Thibert A and Sabio EM *et al.* Evolution of physical and photocatalytic properties in the layered titanates $A_2Ti_4O_9$ (A = K, H) and in nanosheets derived by chemical exfoliation. *Chem Mater* 2009; **22**: 1220–8.
26. Ho W, Jimmy CY and Lee S. Synthesis of hierarchical nanoporous F-doped TiO_2 spheres with visible light photocatalytic activity. *Chem Commun* 2006: 1115–7.
27. Zhang N, Li X and Ye H *et al.* Oxide defect engineering enables to couple solar energy into oxygen activation. *J Am Chem Soc* 2016; **138**: 8928–35.
28. Guo F, Shi W and Zhu C *et al.* CoO and g-C_3N_4 complement each other for highly efficient overall water splitting under visible light. *Appl Catal B* 2018; **226**: 412–20.
29. Giotta L, Mastrogiacomo D and Italiano F *et al.* Reversible binding of metal ions onto bacterial layers revealed by protonation-induced ATR-FTIR difference spectroscopy. *Langmuir* 2011; **27**: 3762–73.
30. Zeng L, Li K and Wang H *et al.* CO oxidation on Au/alpha-Fe_2O_3-hollow catalysts: general synthesis and structural dependence. *J Phys Chem C* 2017; **121**: 12696–710.
31. Xu JQ, Li XD and Liu W *et al.* Carbon dioxide electroreduction into syngas boosted by a partially delocalized charge in molybdenum sulfide selenide alloy monolayers. *Angew Chem Int Ed* 2017; **56**: 9121–5.
32. Wu J, Li XD and Shi W *et al.* Efficient visible-light-driven CO_2 reduction mediated by defect-engineered BiOBr nanosheets. *Angew Chem Int Ed* 2018; **57**: 8719–23.
33. Jiao XC, Li XD and Jin XY *et al.* Partially oxidized SnS_2 nanosheets achieving efficient visible-light-driven CO_2 reduction. *J Am Chem Soc* 2017; **139**: 18044–51.
34. Li XD, Sun YF and Xu JQ *et al.* Selective visible-light-driven photocatalytic CO_2 reduction to CH_4 mediated by atomically thin $CuIn_5S_8$ layers. *Nat Energy* 2019; **4**: 690–9.